UC San Diego

UC San Diego Previously Published Works

Title

Discovery and structural characterization of a therapeutic antibody against coxsackievirus A10

Authors

Zhu, Rui
Xu, Longfa
Zheng, Qingbing
et al.

Peer reviewed

VIROLOGY

Discovery and structural characterization of a therapeutic antibody against coxsackievirus A10

Rui Zhu[1]*, Longfa Xu[1]*, Qingbing Zheng[1]*, Yanxiang Cui[2,3]*, Shaowei Li[1]*, Maozhou He[1], Zhichao Yin[1], Dongxiao Liu[1], Shuxuan Li[1], Zizhen Li[1], Zhenqin Chen[1], Hai Yu[1], Yuqiong Que[1], Che Liu[1], Zhibo Kong[1], Jun Zhang[1], Timothy S. Baker[4], Xiaodong Yan[1,4†], Z. Hong Zhou[2,3†], Tong Cheng[1†], Ningshao Xia[1†]

Coxsackievirus A10 (CVA10) recently emerged as a major pathogen of hand, foot, and mouth disease and herpangina in children worldwide, and lack of a vaccine or a cure against CVA10 infections has made therapeutic antibody identification a public health priority. By targeting a local isolate, CVA10-FJ-01, we obtained a potent antibody, 2G8, against all three capsid forms of CVA10. We show that 2G8 exhibited both 100% preventive and 100% therapeutic efficacy against CVA10 infection in mice. Comparisons of the near-atomic cryo–electron microscopy structures of the three forms of CVA10 capsid and their complexes with 2G8 Fab reveal that a single Fab binds a border region across the three capsid proteins (VP1 to VP3) and explain 2G8's remarkable cross-reactivities against all three capsid forms. The atomic structures of this first neutralizing antibody of CVA10 should inform strategies for designing vaccines and therapeutics against CVA10 infections.

INTRODUCTION

Coxsackievirus A10 (CVA10), a member of the enterovirus species A (EV-A; family *Picornaviridae*), has become one of the major causative agents of hand, foot, and mouth disease (HFMD) and herpangina (HA) in children worldwide (1). Outbreaks of HFMD/HA associated with CVA10 recently occurred in Asia (2–5), Africa (6), and Europe (7–9). For example, a local outbreak was recorded in the Fujian Province of China as recently as 2014, which led to the isolation of the CVA10-FJ-01 strain used in this study. CVA10 infections can lead to typical clinical symptoms of HFMD as well, and some serious complications such as onychomadeses (9, 10), hyperCKemia (11), convulsion (12), central nervous system disorders (12, 13), and even death (14). Furthermore, HFMD surveillance data confirmed the upward trend in its cocirculation with other enteroviruses, such as enterovirus 71 (EV71), CVA16, and CVA6, which have caused more severe clinical outcomes (9). Although CVA10 has reemerged as a considerable global public health threat, no cure or vaccine is yet available.

CVA10 belongs to the *Picornaviridae*, a large family of nonenveloped, small (~30 nm in diameter), plus-strand RNA viruses with an icosahedral capsid (1). An effective therapeutic approach is to develop neutralizing antibodies (NAbs), as has been demonstrated for influenza A virus (15) and Zika virus (16). The atomic structures of virus-NAb complexes allow the identification of viral epitopes, which are critical for rational vaccine development and for understanding mechanisms of virus neutralization (17–19). However, such an approach has yet to be explored for CVA10. It is well known that

picornaviruses generally undergo several steps of structural transition during assembly and infection: procapsid, mature virion, A-particle, and empty particle (20–23). Neutralization can occur at multiple steps during infection at different phases of viral entry and spread (24). NAbs have been shown to promote untimely uncoating of the virus and premature genome release in picornavirus EV71 and human rhinovirus (HRV) (19, 25). Because of the lack of knowledge about the existence of, and similarities/differences among, the multiple capsid forms of CVA10, whether NAbs can cross-react with different forms of particles, or influence transitions between them, is unknown.

Here, we report the immunological and structural characterizations of the isolated CVA10 procapsid, A-particle, and mature virion, each of which has the potential to be an ideal vaccine candidate, particularly the mature virion because it has the strongest antigenicity. Furthermore, we have also identified and characterized a CVA10-specific NAb, named 2G8, we demonstrate not only its high binding efficiency and potent neutralization activity but also strong preventive and therapeutic efficacy against CVA10 infection. In addition, our structural and functional studies show that NAb 2G8 cross-reacts with three forms of capsids and binds at a border region spanning all three viral proteins, VP1 to VP3. The atomic details revealed for the CVA10 antigenic sites and NAb 2G8 can inform vaccine and therapeutic design.

RESULTS

CVA10 mature virion as a viable vaccine candidate

The CVA10 strain CVA10-FJ-01 (GenBank accession no. KY012321) was cultivated in human rhabdomyosarcoma (RD) cells. Three types of particles, corresponding to the bottom, middle, and top bands, were isolated and purified by centrifugation, polyethylene glycol (PEG) precipitation, ultracentrifugation, and ultrafiltration. SDS–polyacrylamide gel electrophoresis (SDS-PAGE) showed that the particles in the bottom band (lane 1) are composed of four capsid proteins, VP1 to VP4 (Fig. 1A). These particles contain RNA genome, which are verified with a $\lambda_{260}/\lambda_{280}$ absorbance ratio of 1.76

[1]State Key Laboratory of Molecular Vaccinology and Molecular Diagnostics, National Institute of Diagnostics and Vaccine Development in Infectious Diseases, School of Life Science, School of Public Health, Xiamen University, Xiamen 361102, P.R. China. [2]California NanoSystems Institute, University of California, Los Angeles, Los Angeles, CA 90095, USA. [3]Department of Microbiology, Immunology, and Molecular Genetics, University of California, Los Angeles, Los Angeles, CA 90095, USA. [4]Department of Chemistry and Biochemistry and Division of Biological Sciences, University of California, San Diego, San Diego, CA 92093–0378, USA.
*These authors contributed equally to this work.
†Corresponding author. Email: nsxia@xmu.edu.cn (N.X.); tcheng@xmu.edu.cn (T.C.); hong.zhou@ucla.edu (Z.H.Z.); xdy@ucsd.edu (X.Y.)
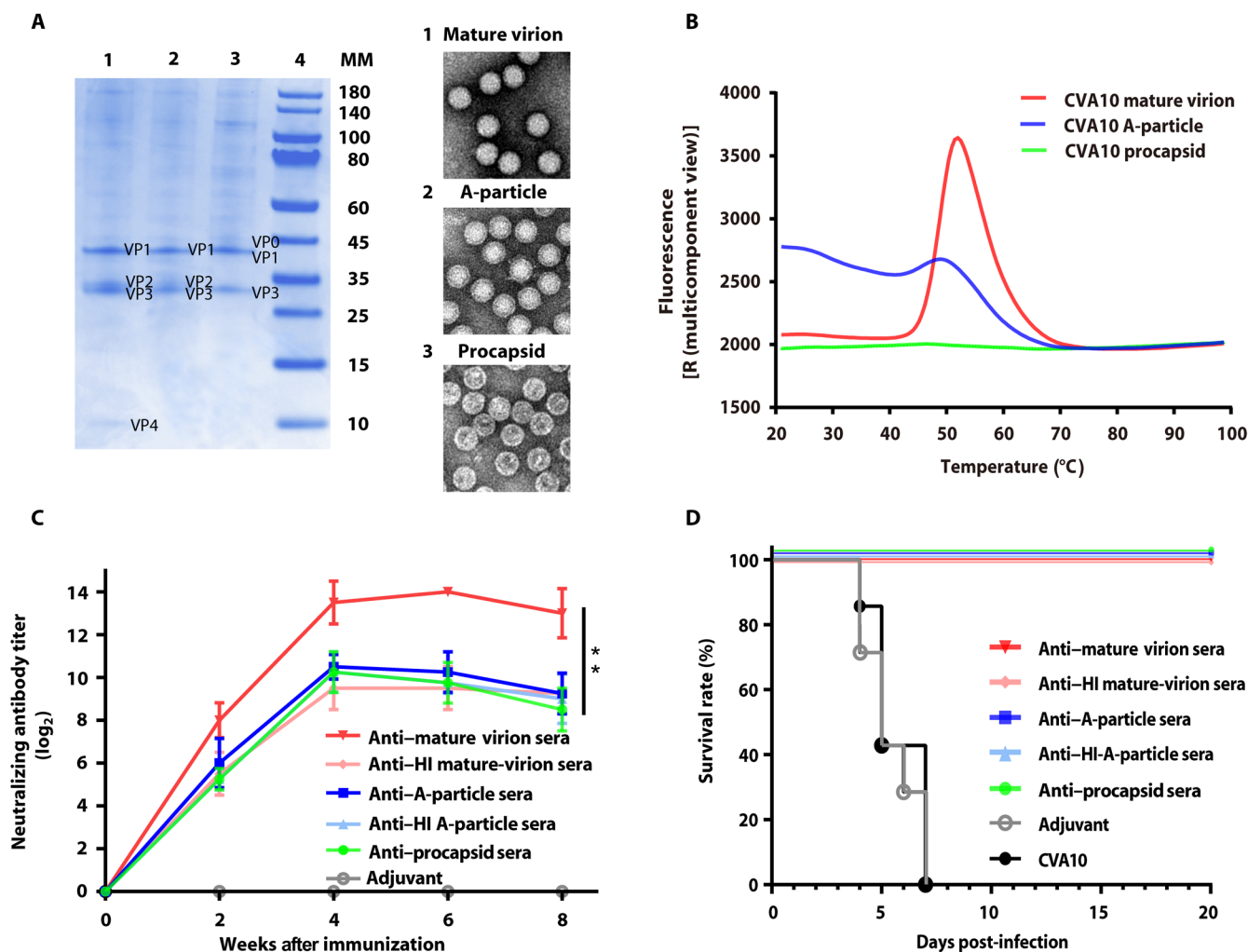
Fig. 1. Stability and immunogenicity of CVA10 particles. (**A**) The SDS-PAGE analysis and negative staining EM of the three types of CVA10 particles. Lane 1, mature virions; lane 2, A-particles; lane 3, procapsids; and lane 4, molecular mass (MM) markers (in kilodaltons). Protein components of each type of particles are labeled along the right side of each lane. The genome is present in both mature virions and A-particles but absent in procapsids. (**B**) The genome exposure and thermal stability of CVA10 particles determined by PaSTRy. The high fluorescence value throughout the whole temperature range indicates that the genome in the A-particle is more exposed than the one in the mature virion. (**C**) In vitro neutralizing titer of antisera of CVA10 particles. BALB/c mice were vaccinated intraperitoneally with CVA10 mature virions, HI mature virions, A-particles, HI A-particles, procapsids, and adjuvant (control) at weeks 0 and 3. Mice were bled at weeks 0, 2, 4, 6, and 8 for neutralization assays, and the levels of neutralizing titers of antisera are expressed as means ± SD. Statistical significance is determined by Mann-Whitney test (**$P < 0.01$). (**D**) In vivo protective efficacy of antisera of CVA10 particles. The infected mice were treated with antisera and were monitored daily for clinical illness and death. All experimental groups showed 100% survival rates, but 0% for two control groups.

and with electron microscopy (EM) images of negative-stained samples (Fig. 1A) and vitrified specimens (fig. S1A). In contrast, the middle (lane 2) and top (lane 3) bands show no trace of VP4 in gel electrophoresis (Fig. 1A) and give $\lambda_{260}/\lambda_{280}$ absorbance ratios of 1.54 and 0.76, respectively, and the negative staining and cryo-EM further confirmed the presence of RNA in the middle band but its absence in the top band (Fig. 1A and fig. S1, B and C). In addition, the release of RNA and stability of particles were explored with the particle stability thermal release assay (PaSTRy). A significant exposure of RNA occurred at ~25°C in the particles of the middle band versus at ~55°C in those of the bottom band, which indicates that the former is less stable than the latter (Fig. 1B). Together, these characteristics suggest that the bottom, middle, and top bands correspond to mature virions, A-particles, and procapsids, respectively.

The immunogenicity of CVA10 was investigated by vaccinating mice separately with purified mature virions, heat-inactivated (HI) mature virions, A-particles, HI A-particles, or procapsids. Antisera harvested from all treated mice at 2-week intervals were tested with an in vitro neutralization assay. Antisera collected from all experimental groups show high and comparable average neutralization titers (Fig. 1C). In particular, mature virions exhibited about 13-fold higher titer than the other groups at week 8, indicating that mature virions are the most immunogenic and can elicit the highest NAb titer. In addition, the in vivo protective efficacy of antisera against CVA10 infection was evaluated using the neonatal mouse model (26). Antisera from all groups of immunized mice showed 100% treatment efficacy, but the mice in control groups started to show signs of illness at 4 days post-infection (d.p.i.) and all died within 7 d.p.i.

(Fig. 1D). Therefore, in terms of strong antigenicity and potent therapeutic efficacy of antisera, all three types of particles, particularly the mature virions, could serve as promising vaccine candidates against CVA10 infection.

Characterization of anti-CVA10 NAb 2G8

A monoclonal antibody (mAb) against CVA10, named 2G8, which exhibits high neutralizing activity in the neutralization assay in vitro [median inhibitory concentration (IC_{50}) = 0.2 μg/ml] (Fig. 2A), was selected for subsequent characterization. 2G8 exhibits high binding efficiency with CVA10 virions, A-particles, or procapsids in enzyme-linked immunosorbent assay (ELISA) tests (Fig. 2B). In addition, murine CVA10 antisera and CVA10-positive human antisera were subjected to a competitive binding efficiency test against 2G8. Both sera show high blocking rates against 2G8 binding to CVA10 particles ranging between 65.0 and 92.4% (Fig. 2C).

The in vivo preventive and therapeutic efficacies of 2G8 were evaluated in neonatal mice challenged with CVA10. NAb 2G8 (dose = 30 μg/g) was administered either before or after mice were challenged with CVA10 viruses [dosage = 10^7 median tissue culture infectious dose ($TCID_{50}$)]. The mice in the control group started to show signs of illness at 4 d.p.i. and all died within 8 d.p.i.; in contrast, all of the animals in both preventive and therapeutic groups survived (Fig. 2D).

Whether NAb 2G8 neutralizes the CVA10 virus in its pre- or post-attachment step during infection was tested by mixing NAb 2G8 with the CVA10 virus either before or 1 hour after the addition of host cells. The neutralizing potency of 2G8 in the pre-attachment assay was about 10 times higher than that in the post-attachment assay (Fig. 2E). As further demonstrated in the cell-based reverse transcription polymerase chain reaction (RT-PCR) assay, the number of virus particles attached to host cells was inversely correlated with the input concentration of 2G8 (Fig. 2F). Hence, 2G8 manifests higher inhibitory capacity in pre-attachment as opposed to post-attachment virus cell binding.

Comparisons of CVA10 mature virion, A-particle, and procapsid structures

Each of the particles corresponding to the three bands separated by ultracentrifugation was vitrified and imaged by low-dose cryo-EM methods (fig. S1, A to C), and the acquired images were subjected to single-particle analysis with the program RELION. As revealed by two-dimensional (2D) and 3D classification results, ~30% of the particles in the bottom band were mature virions and the remaining ~70% were A-particles (fig. S1, F and G). These purified particles were stored at 4°C before vitrification, which indicates that CVA10 mature virions can transform into A-particles in the absence of treatments with low pH or heat. The subsequent 3D reconstructions of the mature virion, A-particle (bottom band), A-particle* (middle band), and procapsid yielded final density maps with estimated resolutions of 3.4, 3.4, 3.6, and 4.0 Å, respectively (Fig. 3, A to C; figs. S2, A and B, and S3; and Table 1). The mature virion map reveals a pseudo T = 3 icosahedral capsid structure with a maximum diameter of ~315 Å along the fivefold axis (Fig. 3A). The A-particle maps are essentially identical with a correlation coefficient of 0.97 (fig. S2C), and hence, to simplify further analysis, the map of A-particle from the bottom band (3.4 Å) was the subject of subsequent studies. The A-particle and procapsid also share an essentially identical, expanded capsid structure (correlation coeffi-

cient, 0.95), with a larger diameter of ~330 Å than that of the mature virion (Fig. 3, B and C). Both expanded particles show open channels at the icosahedral twofold axes (Fig. 3, B and C). In addition, the encapsidated RNA genome is present in the mature virion and A-particle but absent in the procapsid (fig. S4, A to C).

The three density maps at near-atomic resolution allowed us to build atomic models of each of the three particle types (Table 1). The mature virion contains densities attributable to all four capsid proteins (VP1 to VP4), whereas the A-particle and procapsid lack identifiable density corresponding to VP4 (table S1). As in the case of CVA6 (17), the existence of VP0 (that is, the precursor of VP2 and VP4) in the procapsid particle was verified by gel electrophoresis (Fig. 1A), but the density of the VP0 sequence corresponding to VP4 was unidentifiable in the near-atomic resolution cryo-EM map. Superposition of asymmetric units (protomers) of atomic models verifies the similar capsid structures of the A-particle and procapsid [overall root mean square deviation (RMSD) = 0.57 Å in Cα atoms; table S2]. However, the mature virion differs significantly from the A-particle (RMSD = 1.12 Å in Cα atoms between protomers; table S2). The differences are mostly located at the VP1 N terminus and in the surface loops (BC, DE, HI, and GH) close to the icosahedral fivefold axes, and the RMSD value for Cα atoms in VP1 is 1.52 Å (Fig. 3, D and E, and table S2). In addition, the VP3 BC loop of the mature virion is shifted slightly compared with that of the A-particle or procapsid (Fig. 3F). These surface loops, particularly the VP1 loops, have been shown to be the critical antigenic epitopes in many picornaviruses, such as EV71 (27), CVA6 (17), foot and mouth disease virus (28), and HRV (29). Hence, the differences of antigenic determinants among three types of particles explain why the mature virion of CVA10 confers different immunogenicity from the other two.

Structure comparisons between the CVA10 mature virion and other enteroviruses

The overall structure of the CVA10 mature virion is similar to the virions of other representative enteroviruses [EV71 (22), CVA16 (30), CVB3 (31), poliovirus (32), and EVD68 (33)] (Fig. 3G and fig. S5), and the RMSD values range from 0.79 to 1.73 Å between Cα atoms in a protomer (table S2). The CVA10 mature virion closely resembles CVA16 (RMSD = 0.79 Å) and EV71 (RMSD = 0.90 Å), both of which belong to EV-A. This similarity includes the hydrophobic pockets (Fig. 3H) and even the embedded pocket factors (Fig. 3I), which play a critical role in initiating the viral uncoating process (22). However, the pocket regions are recognizably different when CVA10 is compared with CVB3 (species B), poliovirus (species C), or EVD68 (species D) (Fig. 3, H and I). A similar case occurs at the "canyon" regions as well, which usually offer the binding sites for host receptor(s) and primarily comprise VP1 BC and GH loops and the VP2 EF loop (fig. S6A). Overall, the canyon conformation of CVA10 is similar to that of EV71 and CVA16, but different from those of non–species A enteroviruses (fig. S6, B to F). The VP2 EF loop of the CVA10 mature virion slightly extends inward, leading to a narrower distal part of the canyon (fig. S6). In addition, the VP1 GH loop (the south part of the canyon) of CVA10 extends further to form the front part of the canyon, which is flatter than that observed in CVB3, poliovirus, and EVD68 (fig. S6, D to F). Notably, because density attributed to the VP1 BC loop is smeared in the cryo-EM density map of the CVA10 mature virion, the BC loop was excluded from the atomic model.
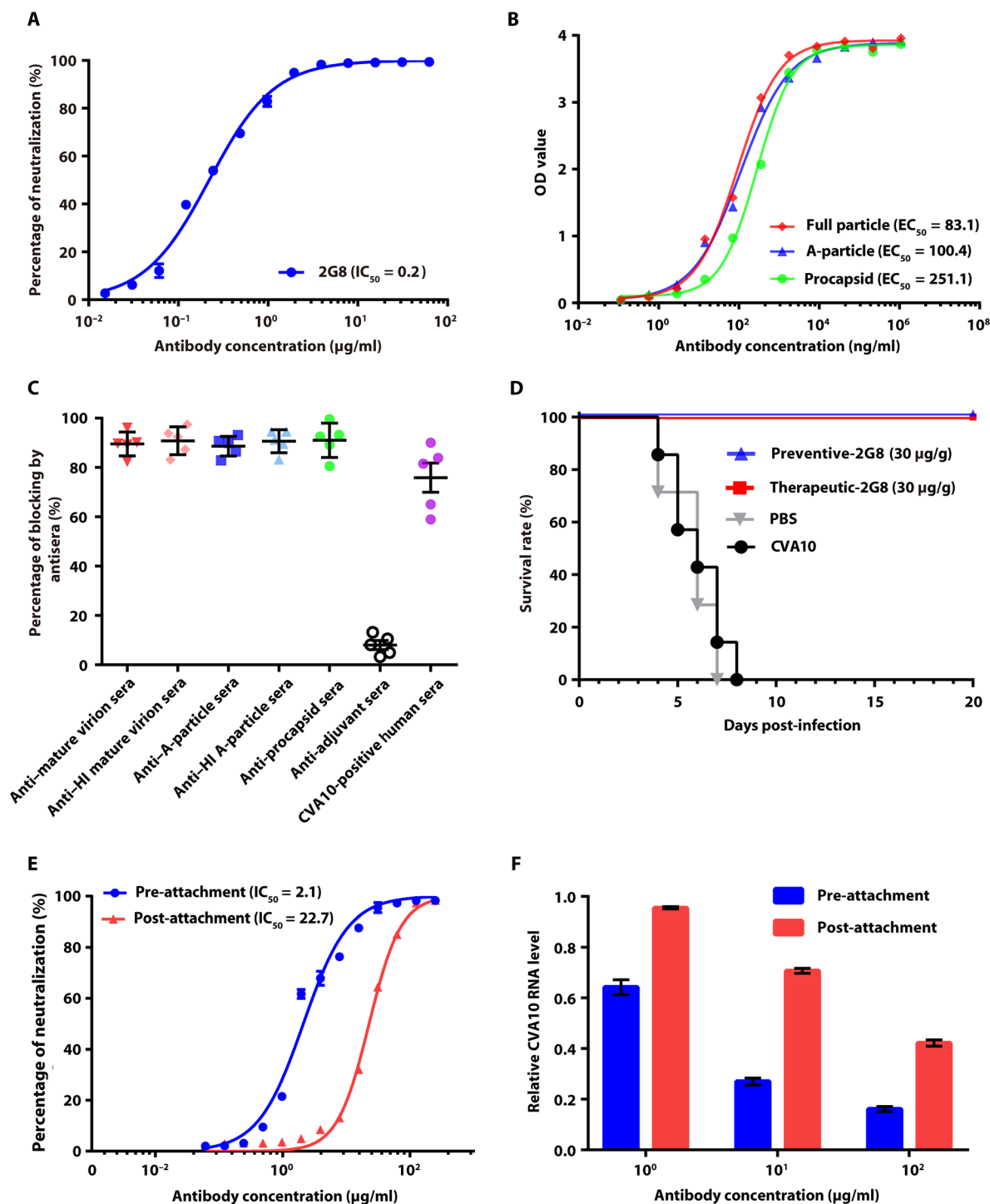
Fig. 2. Characterizations of NAb 2G8. (**A**) Neutralization assay of CVA10 NAb 2G8. The IC_{50} value is 0.2 μg/ml. (**B**) Binding efficacy of NAb 2G8 evaluated with the indirect ELISA. NAb 2G8 exhibits high binding affinities with the CVA10 particles [median effective concentration (EC_{50}) values from 83.1 to 251.1 ng/ml]. The IC_{50} and EC_{50} values were calculated with nonlinear regression fitting curves. The optical density (OD) value was read at $A_{450/620}$. (**C**) The competitive ELISA of NAb 2G8. The binding of NAb 2G8 to CVA10 particles was significantly blocked by sera from mice immunized with CVA10 and CVA10-positive human sera. The percentages of blocking are expressed as means ± SD. (**D**) In vivo preventive and therapeutic efficacy of NAb 2G8. The infected mice were treated with NAb 2G8 12 hours before (blue line) or 24 hours after (red line) infection intraperitoneally with CVA10 and monitored daily after inoculation. Both experimental groups showed 100% survival rates, but 0% for two control groups. (**E**) Neutralization assay of NAb 2G8 at pre-attachment (blue line) or post-attachment (red line). NAb 2G8 exhibits much higher neutralizing capacity at pre-attachment (IC_{50} = 2.1 μg/ml) than at post-attachment (IC_{50} = 22.7 μg/ml). (**F**) Amount of cell-bound CVA10 viruses detected by RT-PCR. Indicated with the relative CVA10 genome level, the amount of cell-bound viruses gradually decreased as a function of increasing NAb 2G8 concentrations in both cases of pre- and post-attachment. Values are expressed as means ± SD. Experiments were repeated in triplicate. PBS, phosphate-buffered saline.
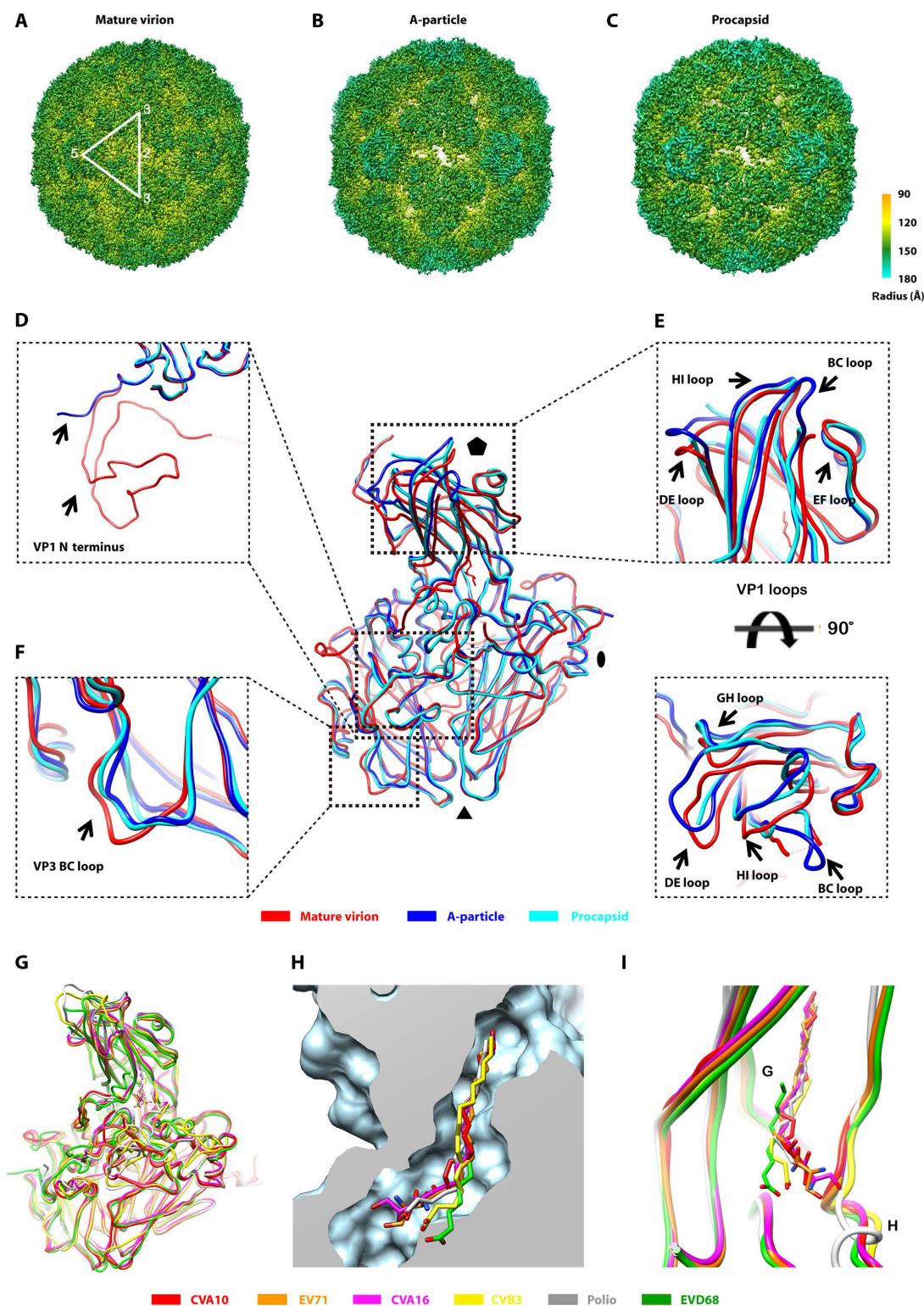
Fig. 3. Atomic structures of the CVA10 mature virion, A-particle, and procapsid. (**A** to **C**) The isocontoured display of cryo-EM density maps (radially colored) of mature virion (A), A-particle (B), and procapsid (C) viewed along a twofold axis. One icosahedral asymmetric unit and icosahedral axes are labeled with a white triangle and numbers. (**D** to **F**) Superpositions (a protomer) of the CVA10 mature virion (red), A-particle (blue), and procapsid (cyan). The differences are mainly located at the VP1 N-termini (D), the VP1 loops (BC, DE, HI and GH) close to fivefold axes (E), and the VP3 BC loop (F). (**G**) Superpositions (a protomer) of mature virions of CVA10 (red), EV71 (orange), CVA16 (magenta), CVB3 (yellow), poliovirus (gray), and EVD68 (green). (**H**) Cutaway view of all the pocket factors (represented with sticks) in (G) situated in a "pocket" (light blue) of the CVA10 mature virion. (**I**) Back view of (H) without the pocket density. The CVA10 mature virion resembles CVA16 and EV71 much more than it does CVB3, poliovirus, and EVD68.

Table 1. Statistics of 3D reconstructions and model refinements. RMS, root mean square.

	Mature virion (CVA10-M)	A-particle (CVA10-A)	A-particle* (CVA10-A*)	Procapsid (CVA10-P)	CVA10-M-2G8	CVA10-A-2G8	CVA1-P-2G8
Data collection							
Microscope	Titan Krios	Titan Krios	Tecnai F30	Tecnai F30	Tecnai F30	Tecnai F30	Tecnai F30
Voltage (kV)	300	300	300	300	300	300	300
Detector	K2	K2	Falcon II	Falcon II	Falcon II	Falcon II	Falcon II
Pixel size (Å)	1.36	1.36	1.128	1.128	1.128	1.128	1.128
Electron dose (Å^2)	60	60	25	25	25	25	25
Frames	60	60	17	17	17	17	17
Defocus range (μm)	0.5–4.7	0.5–4.7	0.6–4.3	0.7–4.4	0.4–5.9	0.4–5.9	0.5–5.7
Reconstruction							
Software				RELION 2.0			
Number of used micrographs	1792	1792	532	543	1749	1749	1809
Number of used particles	17,092	66,306	9411	21,158	36,555	14,425	24,764
Final resolution (Å)	3.4	3.4	3.6	4.0	3.9	4.3	4.2
Average *B* factor (Å^2)	−153.0	−177.9	−206.9	−271.7	−244.0	−253.0	−276.7
Model building							
Software				Coot			
Refinement							
Software				Phenix			
Model statistics							
Correlation coefficient (around atoms)	0.8495	0.8544	—	0.8685	0.8607	0.8601	0.8685
No. of protein atoms	6304	5083	—	4827	8082	5094	4994
Ramachandran outliers	0.00%	0.00%	—	0.00%	0.00%	0.00%	0.00%
Ramachandran favored	93.27%	92.15%	—	89.7%	87.99%	90.72%	90.18%
Rotamer outliers	0.00%	0.18%	—	0.00%	0.00%	0.00%	0.00%
Cβ deviations	0	0	—	0	0	0	0
Clashscore	2.73	2.49	—	4.71	4.84	2.98	5.78
RMS (bonds)	0.0078	0.0052	—	0.0089	0.0123	0.0077	0.0089
RMS (angles)	1.2	1.2	—	1.3	1.3	1.2	1.3
EMRinger score	4.7	4.1	—	4.1	3.3	3.8	2.8

*A-particle from the middle band.

The capsid structure of the CVA10 A-particle was also similar to that of EV71, CVA16, and CVA6 with RMSD values (Cα atoms in a protomer) of 1.03, 0.85, and 0.62 Å, respectively (table S2). The superposition of four structures reveals that the biggest differences are located at some surface loops of VP1 (BC, DE, EF, and HI) and VP3 (AB and BC). In particular, the VP1 BC loop of the CVA10 A-particle extends further toward the fivefold vertex of the capsid compared to that of EV71, CVA16, and CVA6 (fig. S2, D to F, and table S2).

Cryo-EM reconstructions of CVA10 particles complexed with 2G8

To investigate the molecular determinants of 2G8, we obtained three cryo-EM structures of Fab 2G8 in complex with the CVA10 mature virion (CVA10-M-2G8), A-particle (CVA10-A-2G8), and procapsid (CVA10-P-2G8). The acquired micrographs and subsequent 2D classification of extracted particle images clearly exhibit the presence of extra density features at high radii (fig. S1, D and E). These features

presumed to represent the Fabs had density levels comparable to those of capsid, which suggests that Fab 2G8 bound at near-saturation level. The following 3D image reconstructions yielded density maps with final estimated resolution limits of 3.9 Å (CVA10-M-2G8), 4.3 Å (CVA10-A-2G8), and 4.2 Å (CVA10-P-2G8) (Table 1 and fig. S3). The density maps reveal the same epitope and binding pattern (60 copies of 2G8 per particle) in all three immune complexes (Fig. 4A and figs. S4, D to F, and S7, A to C). The epitope of 2G8 maps to the south rim of the canyon surrounding the quasi-threefold axis, where all three capsid proteins (VP1 to VP3) converge (Fig. 4, B and C).

The cryo-EM density map of CVA10-M-2G8 at near-atomic resolution allowed us to build an atomic model of the capsid and the bound variable domain of the Fab. This model reveals that the Fab-capsid interaction interface projects a footprint across three viral proteins (VP1 to VP3) and buries a total surface area of ~1100 Å^2 on the capsid (Fig. 4C and fig. S7D). Such interface establishes an elaborate network of interactions including 14 hydrogen bonds and nine salt bridges between complementarity-determining regions (CDRs) and the capsid (Fig. 4, D to G, and table S3). All three CDRs in the heavy chain (HCDRs) of the Fab variable domain interact with the capsid at the VP1 C termini, VP2 EF loop, and VP3 AB loop (Fig. 4, D to G, and table S3). In contrast, only one CDR in the light chain (LCDR) interacts with the VP1 C termini.

The lower resolution limits of CVA10-A-2G8 and CVA10-P-2G8 density maps meant that only atomic models of the capsids in these immune complexes were successfully built. The capsid structures in all three immune complexes are essentially identical to the structures of the corresponding unbound particles. These identities are confirmed with the overall RMSD values ranging from 0.42 to 0.86 Å between Cα atoms in one protomer (table S2). The twofold channels are still closed in CVA10-M-2G8 but remain open in both CVA10-A-2G8 and CVA10-P-2G8 (Fig. 5, A to C).

The capsid (protomer) of CVA10-A-2G8 or CVA10-P-2G8 was superimposed onto that of CVA10-M-2G8, which confirmed that the epitope of 2G8 is essentially identical across all three types of particles. Such identity is not accidental in the context of significant differences located at β sheet jelly-roll folds of VP1 and VP3 (Fig. 5D). The epitope of 2G8 sits near the quasi-threefold axis and represents a novel antigenic site (site 4) that barely overlaps any other previously reported neutralization epitopes (sites 1 to 3) of enteroviruses (Fig. 5E). 2G8 can cross-react with three distinct types of particles; thus, this epitope is a structurally well-conserved antigenic site during the life cycle of CVA10.

DISCUSSION

Picornaviruses primarily exist as two capsid forms in infected cells: empty procapsids (noninfectious) and mature virions (infectious) (22, 34). Upon binding with specific receptors, mature virions can transform into a transient form, uncoating intermediates or A-particles, which then become difficult to be isolated from the infected cells (23, 35–37). However, as an anomalous member of the picornavirus family, CVA6 adopts procapsids and A-particles as stable beings in its life cycle (17). Here, the CVA10 procapsid, A-particle, and mature virion were routinely isolated, and a large fraction of the mature virions would transform into A-particles during long-term storage at 4°C. A recent study found that the VP1 BC loop can regulate the assembly and maturation process of EV71

particles and the subsequent conversion from mature virions to A-particles during viral uncoating and replication (38). Comparisons between CVA10 and other enteroviruses indeed revealed significant variation in conformations at the VP1 BC loop (fig. S2F). Hence, the VP1 BC loop of CVA10 seems to play a key role in viral uncoating and capsid transition among different forms of particles.

In CVA16 and hepatitis A virus, the mature virions and procapsids were reported to have similar antigenicity, albeit their structures are distinct from each other (30, 34). As our results show, antisera elicited from all three forms of CVA10 particles showed comparable neutralizing titers, together with the information of structurally defined common epitope across three capsid forms, which indicates that all the particles share some structurally conserved epitopes, for instance, 2G8. Such epitope would be an excellent target for specific antiviral design against CVA10. On the other hand, CVA10 mature virions exhibit stronger antigenicity and more potent therapeutic efficacy than the other two types of particles. Comparisons between the atomic models of CVA10 particles revealed that the VP1 N termini loops close to fivefold axis and the VP3 BC loop probably determine their respective antigenicity.

Previous cryo-EM studies of neutralizing mAb-virion complexes identified several neutralization antigenic sites in poliovirus, EV71, and CVA6, near the rims or the bottom of the canyon and the icosahedral three- or twofold axis (Fig. 5E) (17, 25, 27, 39–41). These neutralizing epitopes can be categorized into four major sites: site 1 (EV71 MA28-7, poliovirus A12, and CVA6 1D5), site 2 (EV71 D5 and 22A12), site 3 (EV71 E18), and site 4 (CVA10 2G8). Site 1 is located at the north rim of the canyon, which overlaps or is adjacent to the binding sites of the host cell receptors (17, 27, 39). Site 2 mainly lies at the VP1 GH loop surrounding the twofold axis. It offers either a monovalent or a bivalent binding pattern of the neutralizing Fabs on EV71 mature virion and procapsid (40, 41). Site 3 lies near the icosahedral threefold axis, and its elicited NAbs can trigger the conversion from EV71 mature virions to A-particles, followed by a premature genome release (25). Here, our immune complex structures reveal that NAb 2G8 defines a novel capsid state cross-neutralization epitope, site 4, including the VP1 C termini, VP2 EF loop, and VP3 AB loop adjacent to the quasi-threefold channel on the CVA10 procapsid, mature virion, or A-particle. Researchers have reported a channel at the quasi-threefold axis and a larger opening at the twofold axis in the A-particles, either of which would allow the exit of the VP1 N termini, VP4, and viral RNA genome (22, 23). Therefore, NAb 2G8 may neutralize CVA10 particles in a manner that restricts the necessary conformational changes at the quasi-threefold channels that would otherwise lead to the release of the polypeptide chain and RNA genome.

Our study provides atomic-level information about molecular determinants of viral structure transitions, similar antigenicity, and conserved epitope, which are based on three capsid states of CVA10 and immune complexes. Because NAb 2G8 can cross-react with all three forms of particles, its epitope can serve as a crucial target for vaccine design or NAb-based therapeutics against CVA10 infection.

MATERIALS AND METHODS
Virus production and purification
The CVA10 strain CVA10-FJ-01 (GenBank accession no. KY012321) had been isolated from a clinical patient in 2014 in Fujian Province and
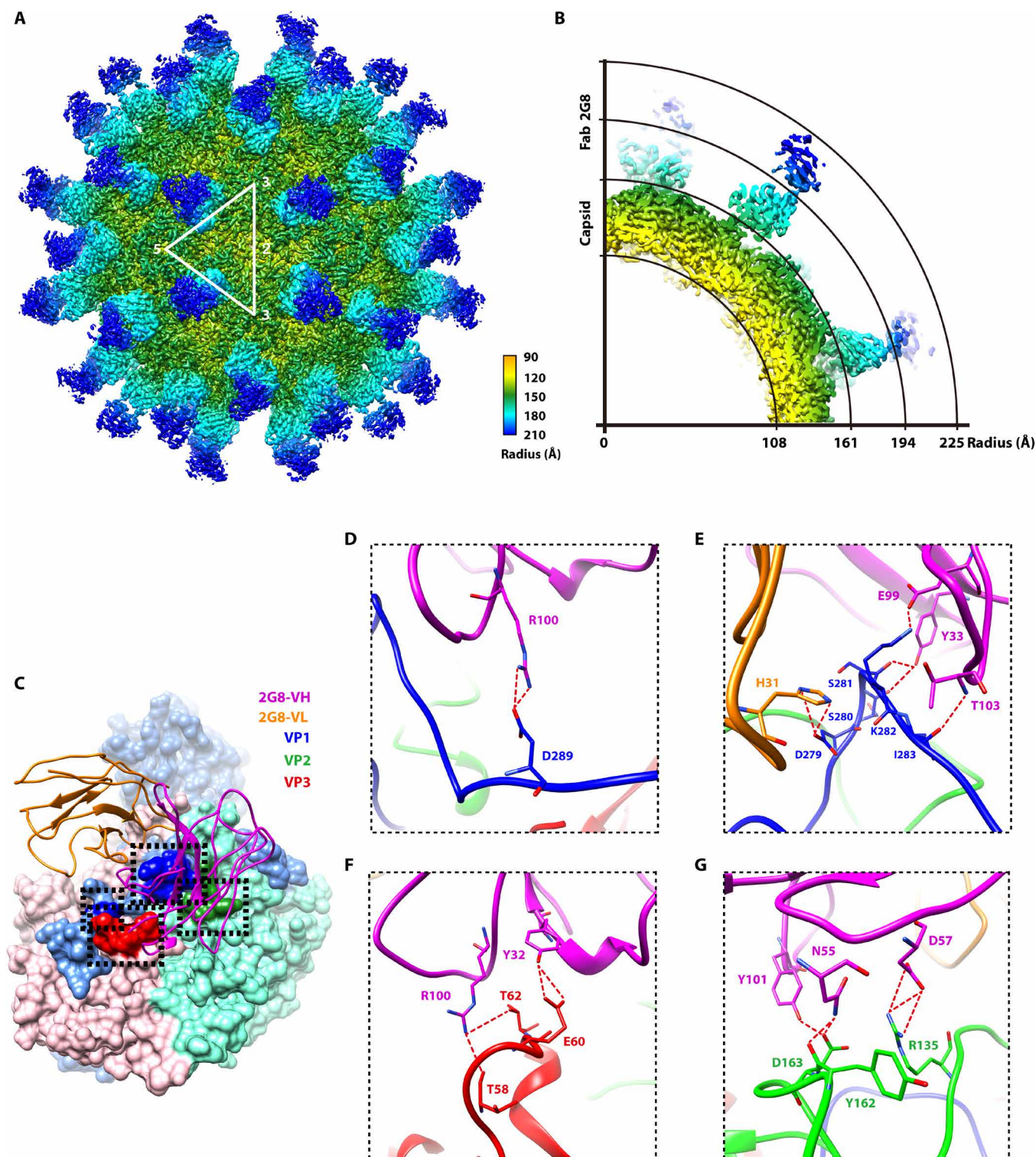
Fig. 4. Atomic structure of the CVA10 mature virion complexed with Fab 2G8. (**A**) The isocontoured display of the cryo-EM density map (radially colored) of the immune complex CVA10-M-2G8 viewed along an icosahedral twofold axis. One icosahedral asymmetric unit and icosahedral axes are labeled with a white triangle and numbers. (**B**) A quarter of the central cross section of (A) exhibiting the densities of capsid (yellow to green) and Fab 2G8 (cyan to blue). The radii are marked by the arcs. (**C**) Surface representation of a protomer in (A) showing the interaction interface between Fab 2G8 (ribbon diagram) and the capsid. Only the variable domain (light chain, orange; heavy chain, magenta) of 2G8 is displayed. The capsid proteins VP1 to VP3 are colored light blue, light green, and light red, but the surface on the capsid covered by the footprint of the Fab 2G8 is respectively highlighted in their darker colors. (**D** to **G**) Expanded views of interaction interface spotlighting the VP1 C terminus (D and E), VP3 AB loop (F), and VP2 EF loop (G). Presumable hydrogen bonds and salt bridges in the interaction interface are marked by red dashed lines.
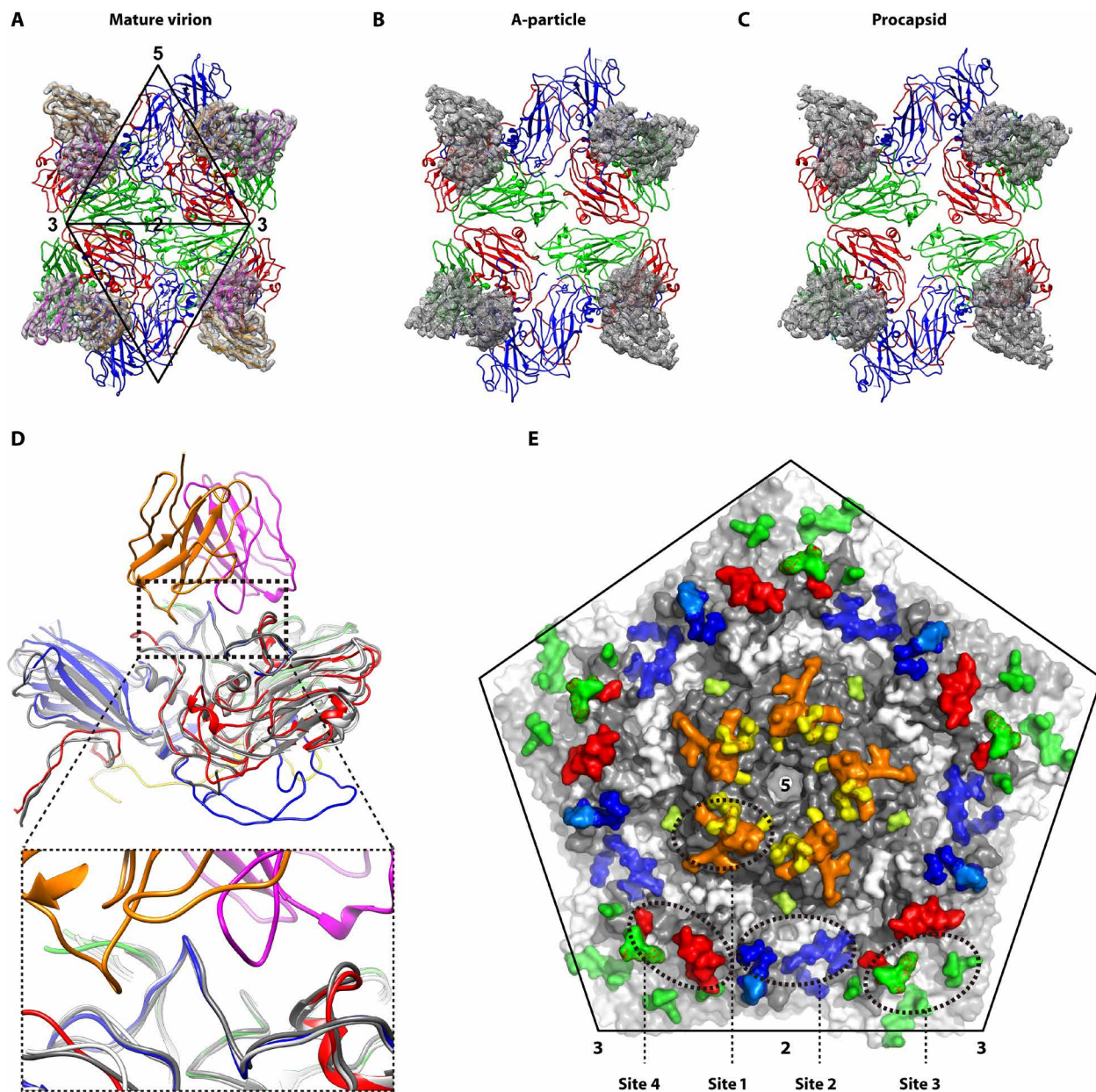
Fig. 5. Structure comparisons between three types of CVA10 particles complexed with Fab 2G8. (**A** to **C**) Views of the regions surrounding an icosahedral twofold axis of immune complex structures of CVA10-M-2G8 (A), CVA10-A-2G8 (B), and CVA10-P-2G8 (C). Two asymmetric units and icosahedral axes are labeled with two black triangles and numbers in (A). Capsid proteins are displayed in ribbon diagrams, while variable domains of Fab 2G8 are displayed in cryo-EM densities (gray). The atomic model of the variable domain is also shown in (A). (**D**) The superposition of capsid proteins of three immune complexes demonstrating the consistency of the epitope across three types of CVA10 particles. The atomic models of capsid proteins from CVA10-M-2G8 and variable domains of Fab 2G8 are shown in colored ribbons, but capsid proteins of CVA10-A-2G8 and CVA10-P-2G8 are respectively shown in gray and white. (**E**) Reported epitopes of enteroviruses mapped onto the CVA10 density map showing only the surface region encircling an icosahedral fivefold axis. All these epitopes are classified into four antigenic sites (sites 1 to 4) surrounding two sides of the canyon. Site 1 represents epitopes in EV71 MA28-7 (yellow), CVA6 1D5 (orange), and poliovirus-A12 (lemon). Site 2 indicates the epitopes in EV71 D5 (blue) and EV71 22A12 (marine). Site 3 belongs to the epitope in EV71 E18 (green). The epitope of 2G8 is uniquely located at site 4.

was grown in RD cells (American Type Culture Collection, CCL-136) at a multiplicity of infection of 0.1. Infected cells were incubated at 37°C for 3 days and centrifuged at 7000*g* for 30 min to remove cell debris. The virus in the supernatant was precipitated using 6% (w/v) PEG 8000 in PBS buffer (pH 7.4). After one more centrifugation, the virus was resuspended in PBS buffer and subsequently loaded onto a 15 to 45% (w/v) sucrose density gradient for ultracentrifugation in a Beckman SW41 Ti rotor at 150,000*g* for 3.8 hours. The virus bands were individually collected and dialyzed against PBS buffer. Then, the virus was concentrated with cutoff filters. All steps of the purification procedure were carried out at 4°C. The purity of virus preparation was assessed with Coomasie-stained SDS-PAGE gel (NuPAGE 4-12% Bis-Tris Gel, Invitrogen).

Particle stability thermal release assay

ThermoFluor assay (42) was performed with an MX3005P RT-PCR instrument (Agilent/Stratagene). The presence of single-stranded RNA was detected with SYTO9 (Invitrogen) as a fluorescent probe. Each 50-μl reaction mixture, containing 1 μg of virus and 5 μM SYTO9 in PBS buffer, was set up in thin-walled PCR plates (Agilent). The fluorescence level was recorded in triplicate at temperatures between 25° and 99°C at 0.5°C intervals.

Vaccine preparation and immunization of mice

The immunogenicity of the CVA10 virus was evaluated in BALB/c mice. The purified CVA10 mature virions and A-particles were inactivated by heating at 56°C for 30 min. Viruses were diluted in PBS and mixed with an equal volume of aluminum adjuvant. Groups of mice (n = 5) were respectively vaccinated with mature virions, HI mature virions, A-particles, HI A-particles, procapsids, or aluminum adjuvant (control) at weeks 0 and 3. Each mouse was intraperitoneally injected with 0.5 ml of the samples at 2.5 μg per dose. Antisera elicited from all groups were inactivated by incubation at 56°C for 30 min and stored at −20°C. All animal experiments were approved by the Institutional Animal Care and Use Committee and Laboratory Animal Management Ethics Committee at Xiamen University.

Preparation of antibodies and antibody fragments

To obtain the anti-CVA10 mAb 2G8, BALB/c mice were immunized subcutaneously with CVA10 mature virions emulsified in an equal volume of Freund's adjuvant (Sigma-Aldrich) and boosted twice at 2-week intervals. After the final boost, spleen cells from immunized mice were fused with Sp2/0 myeloma cells, and the obtained hybridoma supernatants were screened by indirect ELISA and neutralization assay against CVA10. Antibody 2G8 was purified from mouse ascetic fluid produced from single-positive cells by protein A chromatography (GE Healthcare). To prepare the Fab fragment, mAb 2G8 was digested at 37°C for 12 hours with papain at 1% (per mil) (w/w) in PBS buffer, containing 0.01 M L-cysteine and 0.05 M EDTA. The digestion was terminated with the addition of 0.03 M iodoacetamide. Fab fragments were then purified with a DEAE column (Tosoh). The variable domains of both heavy and light chains were sequenced by PCR amplification.

In vitro neutralization assay

RD cells were preseeded in 96-well plates with 1×10^4 cells per well. Antisera or mAb 2G8 was serially diluted twofold and incubated with an equal volume of CVA10 (100 TCID$_{50}$ per well) at 37°C for 1 hour. The mixtures were then added to cells and incubated at 37°C for 5 to 7 days. The cytopathic effect (CPE) was observed with microscopy, and a neutralizing titer was defined as the highest dilution giving >50% neutralization of the well. A neutralizing titer of antisera with values of ≥1:8 was considered as a threshold for positivity.

ELISA
Binding ELISA

The purified CVA10 full particles (mature virions:A-particles ≈ 3:7), A-particles, and procapsids were respectively diluted in PBS buffer and coated onto 96-well ELISA plates with 50 ng of viruses per well. After overnight incubation at 4°C, the plates were washed once with PBST buffer (0.05% Tween 20 in PBS buffer) and saturated with the saturation buffer (0.25% casein and 1% gelatin in PBS buffer) at

37°C for 2 hours. mAb 2G8 at various concentrations was then added to the plates, followed by incubation at 37°C for 1 hour. After five washes with PBST buffer, the plates were mixed with horseradish peroxidase–conjugated goat anti-mouse (GAM-HRP; 1:5000 dilution) immunoglobulin G antibody and incubated at 37°C for 30 min. After five more washes, the plates were incubated with a solution of tetramethylbenzidine for 15 min, and the reaction was terminated with 2.1 M H$_2$SO$_4$. Thereafter, the absorption was measured at $A_{450/620}$.

Competitive ELISA

The antisera from mice immunized with CVA10 or CVA10-positive human sera were used for the competitive ELISA. mAb 2G8 was conjugated to HRP using the NaIO$_4$ oxidation method. The HRP-2G8 (1:3000 dilution) was used to block the binding of sera (1:100 dilution) to CVA10 coated on ELISA plates. Percentage inhibition (PI) was calculated with the following formula: PI (%) = 100 − [(OD$_{sample}$/OD$_{control}$) × 100].

In vivo protection assay

In prevention experiments, groups of neonatal mice were inoculated intraperitoneally with 100 μl of either antisera or NAb 2G8 (30 μg for each gram of body weight) 12 hours before intraperitoneal inoculation with 100 μl of CVA10 (10^6 TCID$_{50}$ per mouse). In treatment experiments, mice were simply inoculated intraperitoneally with NAb 2G8 24 hours after inoculation of CVA10. The mice in the control groups were treated with PBS buffer via the same route. Every group comprised 8 to 10 mice. All mice were monitored daily for clinical illness and death until 20 d.p.i.

Pre- and post-attachment neutralization assays

RD cells were preseeded in 96-well plates and ready for two assays. Each incubation in both assays was performed at 4°C with a duration of 1 hour unless otherwise stated. In the pre-attachment neutralization assay, serially diluted mAb 2G8 was incubated with CVA10 and then added to the cells for one more incubation. In the post-attachment neutralization assay, the cells were first incubated with CVA10 and then washed twice with cold PBS buffer. Different dilutions of mAb 2G8 were subsequently added for one more incubation. The cells were finally washed twice with cold PBS buffer and incubated at 37°C for 4 days. The CPE was observed under the microscope.

RT-PCR to quantitate virus on cell surface

The amount of CVA10 particles remaining on the surface of RD cells was estimated by a one-step, quantitative RT-PCR as previously described (17). Some steps of the experimental procedure are similar to the pre- and post-attachment neutralization assay described in the above section. Briefly, CVA10 was mixed with different concentrations of mAb 2G8 either before or after the viruses were coated on preseeded cells. The mixture was then incubated at 4°C for 1 hour. After three washes with cold PBS buffer, total RNA was isolated using the QIAamp Mini Viral RNA Extraction Kit (Qiagen). RT-PCR reaction was performed with the CFX96 Real-Time PCR Detection System (Bio-Rad). Gene-specific primers (forward, 5′-TACTTTG-GGTGTCCGTGTTT-3′; reverse, 5′-TGGCCAATCCAATAGC-TATATG-3′; probe, 5′-FAM- AYTGGCTGCTTATGGTGA-CRAT-BHQ1-3′) were used for the RT-PCR experiment. The relative levels of CVA10 RNA in different samples were estimated by the comparative 2$^{-\Delta\Delta Ct}$ method (43).

Negative staining EM

Purified CVA10 viruses were diluted in PBS buffer and then absorbed onto 200-mesh carbon-coated copper grids for 1 min. The grids were washed twice with double-distilled water and subsequently negatively stained with 2% phosphotungstic acid (pH 6.4) for 30 s. Specimens were evaluated and imaged with the FEI Tecnai T12 transmission electron microscope at a magnification of 25,000×.

Cryo-EM sample preparation and data acquisition

Three types of CVA10 particles (mature virion, A-particle, and procapsid) were purified and stored at 4°C for cryo-EM sample preparation. The CVA10 immune complexes were prepared by mixing Fab 2G8 with CVA10 particles at a molar ratio of 72:1. Mixtures were then incubated at 37°C for 30 min. Aliquots (3 µl) of samples of different viral particles or immune complexes were applied onto glow-discharged holey carbon Quantifoil Cu grids (R2/2, 200 mesh, Quantifoil Micro Tools) inside the FEI Mark IV Vitrobot at a humidity level of 100%, blotted with filter papers for 6 s, and then plunged into liquid ethane cooled by liquid nitrogen. The vitrified specimens were examined under low-dose conditions at 300 kV with the FEI Titan Krios or Tecnai F30. Micrographs acquired with the Krios were recorded on the post-GIF K2 camera at a nominal magnification of 105,000×, corresponding to a calibrated physical pixel size of 1.36 Å (0.68 Å for super-resolution pixel size). The slit width in the Gatan GIF system was set to 20 eV to remove inelastically scattered electrons. Each movie contains 60 subframes with a total exposure time of 12 s (0.2 s for each subframe); the dose rate was set to ~9.5 e$^-$ per physical pixel per second; hence, the total dose of each exposure was ~60 e$^-$/Å^2. Micrographs acquired with the Tecnai F30 were recorded on the Falcon II direct electron detector in the 17-frame movie mode at a nominal magnification of 93,000×, corresponding to a pixel size of 1.128 Å. The total electron dose was set to 25 e$^-$/Å^2, and the total exposure time was 1 s. Micrographs with minimum drift or astigmatism were selected for subsequent image processing.

Image processing

Movie frames were aligned to correct the drift and beam-induced motion with the program MotionCor2 (44), and the contrast transfer function of each aligned micrograph was estimated with the program Gctf (45). Particles from several representative micrographs were manually boxed using the e2boxer.py program from the EMAN 2.1 package (46), which were then used as reference for autopicking particles of whole data set with the program RELION 2.0 (47). All extracted particle images underwent multiple rounds of 2D classifications, and the classes that exhibited identifiable secondary structures features were rated as "good" ones. Particles in good classes were used to generate initial 3D models with the random model method in the program AUTO3DEM (48) and were further processed for 3D image reconstructions with the program RELION 2.0. The resolutions of maps were estimated using gold-standard criteria with the Fourier shell correlation (FSC) cutoff = 0.143 (49). Local resolution variations were estimated using the program ResMap (50).

Model building and refinement

The initial atomic model templates of all three particles and immune complexes were generated from homology modeling upon CVA6 [Protein Data Bank (PDB) code: 5XS4 (17)] and its immune complex [PDB code: 5XS7 (17)] by Accelrys Discovery Studio software (51). Then, the template was docked into a segmented volume (enclosing a promoter) of final cryo-EM maps (viral particles or immune complexes) using Chimera (52). The sequence assignment was guided by the clearly recognizable features for bulky side chains, such as Phe, Tyr, Arg, and Trp. The manual model building and automatic refinement were alternately and iteratively performed in Coot (53) and the module phenix.real_space_refine in PHENIX (53, 54). The refined protomer was docked into the density of six neighboring protomers, which were then treated as a whole model for further optimization to avoid clashes between protomers. Model statistics including bond lengths, bond angles, all atom clashes, rotamer statistics, Ramachandran plot statistics, etc., were closely inspected with Coot during the whole process. The final models were validated using Molprobity (55) and EMRinger (56). Multiple sequence alignments were performed using ClustalW and ClustalX (version 2) on the EBI server, and the results were generated using ESPript (57). Figures were prepared with Chimera (52) and PyMOL (58). The roadmap of Fabs footprint was displayed with the program Radial Interpretation of Viral Electron density Maps (RIVEM) (59). The interactions between virus capsid and Fab were inspected with the software CCP4 (60) and the PISA sever (www.ebi.ac.uk/pdbe/pisa). The intermolecular interactions were analyzed on the basis of the assumption that cutoff distances are 4 Å for a hydrogen bond and 3.5 Å for a salt bridge.

SUPPLEMENTARY MATERIALS

Supplementary material for this article is available at http://advances.sciencemag.org/cgi/content/full/4/9/eaat7459/DC1

Fig. S1. Cryo-EM micrographs of CVA10 particles and CVA10-2G8 complexes, and 3D classification of CVA10 mature virion particles.

Fig. S2. Structure comparisons of A-particles of CVA10, EV71, CVA16, and CVA6.

Fig. S3. Global and local resolution analyses of 3D reconstructions of CVA10 particles and CVA10-2G8 complexes.

Fig. S4. Central sections of density maps of CVA10 particles and CVA10-2G8 complexes.

Fig. S5. ESPript representation of structure-based sequence alignments of VP1, VP2, VP3, and VP4 of CVA10 with six other representative picornaviruses.

Fig. S6. Structure comparisons of the canyon regions between CVA10 and other enteroviruses.

Fig. S7. The cryo-EM density maps of CVA10-2G8 complexes and roadmap of six Fab 2G8 footprints on the CVA10 mature virion capsid.

Table S1. Regions with unidentifiable residues in atomic models.

Table S2. Structure comparisons (RMSD) of CVA10 particles and CVA10 to other enteroviruses.

Table S3. Interaction contacts in the immune complex CVA10-M-2G8.

REFERENCES AND NOTES

1. A. Itagaki, T. Kamahora, T. Kurimura, Isolation and characterization of a cold-sensitive strain of coxsackievirus A10. *J. Gen. Virol.* **68**, 1191–1194 (1987).

2. W. M. Koh, T. Bogich, K. Siegel, J. Jin, E. Y. Chong, C. Y. Tan, M. I. C. Chen, P. Horby, A. R. Cook, The epidemiology of hand, foot and mouth disease in Asia: A systematic review and analysis. *Pediatr. Infect. Dis. J.* **35**, e285–e300 (2016).

3. W. Xing, Q. Liao, C. Viboud, J. Zhang, J. Sun, J. T. Wu, Z. Chang, F. Liu, V. J. Fang, Y. Zheng, B. J. Cowling, J. K. Varma, J. J. Farrar, G. M. Leung, H. Yu, Hand, foot, and mouth disease in China, 2008–12: An epidemiological study. *Lancet Infect. Dis.* **14**, 308–318 (2014).

4. Q. Yang, J. Ding, J. Cao, Q. Huang, C. Hong, B. Yang, Epidemiological and etiological characteristics of hand, foot, and mouth disease in Wuhan, China from 2012 to 2013: Outbreaks of coxsackieviruses A10. *J. Med. Virol.* **87**, 954–960 (2015).

5. R. Zhu, T. Cheng, D. Yin, D. Liu, L. Xu, Y. Li, W. Wang, J. Liu, Y. Que, X. Ye, Q. Tang, Q. Zhao, S. Ge, S. He, N. Xia, Serological survey of neutralizing antibodies to eight major enteroviruses among healthy population. *Emerg. Microbes Infect.* **7**, 2 (2018).

6. V. Gopalkrishna, P. R. Patil, G. P. Patil, S. D. Chitambar, Circulation of multiple enterovirus serotypes causing hand, foot and mouth disease in India. *J. Med. Microbiol.* **61**, 420–425 (2012).

7. A. Mirand, C. Henquell, C. Archimbaud, S. Ughetto, D. Antona, J.-L. Bailly, H. Peigue-Lafeuille, Outbreak of hand, foot and mouth disease/herpangina associated with coxsackievirus A6 and A10 infections in 2010, France: A large citywide, prospective observational study. *Clin. Microbiol. Infect.* **18**, E110–E118 (2012).

8. S. Blomqvist, P. Klemola, S. Kaijalainen, A. Paananen, M.-L. Simonen, T. Vuorinen, M. Roivainen, Co-circulation of coxsackieviruses A6 and A10 in hand, foot and mouth disease outbreak in Finland. *J. Clin. Virol.* **48**, 49–54 (2010).

9. M. A. Bracho, F. González-Candelas, A. Valero, J. Córdoba, A. Salazar, Enterovirus co-infections and onychomadesis after hand, foot, and mouth disease, Spain, 2008. *Emerg. Infect. Dis.* **17**, 2223–2231 (2011).

10. J. L. Davia, P. H. Bel, V. Z. Ninet, M. A. Bracho, F. González-Candelas, A. Salazar, M. Gobernado, I. F. Bosch, Onychomadesis outbreak in Valencia, Spain associated with hand, foot, and mouth disease caused by enteroviruses. *Pediatr. Dermatol.* **28**, 1–5 (2011).

11. H. Okada, M. Wada, H. Sato, Y. Yamaguchi, H. Tanji, K. Kurokawa, T. Kawanami, T. Takahashi, T. Kato, Neuromyelitis optica preceded by hyperCKemia and a possible association with coxsackie virus group A10 infection. *Intern. Med.* **52**, 2665–2668 (2013).

12. M. Chen, S. He, Q. Yan, X. Xu, W. Wu, S. Ge, S. Zhang, M. Chen, N. Xia, Severe hand, foot and mouth disease associated with Coxsackievirus A10 infections in Xiamen, China in 2015. *J. Clin. Virol.* **93**, 20–24 (2017).

13. A. Kumar, D. Shukla, R. Kumar, M. Z. Idris, P. Jauhari, S. Srivastava, T. N. Dhole, Molecular identification of enteroviruses associated with aseptic meningitis in children from India. *Arch. Virol.* **158**, 211–215 (2013).

14. M. E. Fuschino, D. M. Lamson, K. Rush, L. S. Carbone, M. L. Taff, Z. Hua, K. Landi, K. S. George, Detection of coxsackievirus A10 in multiple tissues of a fatal infant sepsis case. *J. Clin. Virol.* **53**, 259–261 (2012).

15. N. L. Kallewaard, D. Corti, P. J. Collins, U. Neu, J. M. McAuliffe, E. Benjamin, L. Wachter-Rosati, F. J. Palmer-Hill, A. Q. Yuan, P. A. Walker, M. K. Vorlaender, S. Bianchi, B. Guarino, A. De Marco, F. Vanzetta, G. Agatic, M. Foglierini, D. Pinna, B. Fernandez-Rodriguez, A. Fruehwirth, C. Silacci, R. W. Ogrodowicz, S. R. Martin, F. Sallusto, J. A. Suzich, A. Lanzavecchia, Q. Zhu, S. J. Gamblin, J. J. Skehel, Structure and function analysis of an antibody recognizing all influenza A subtypes. *Cell* **166**, 596–608 (2016).

16. J. Wang, M. Bardelli, D. A. Espinosa, M. Pedotti, T.-S. Ng, S. Bianchi, L. Simonelli, E. X. Y. Lim, M. Foglierini, F. Zatta, S. Jaconi, M. Beltramello, E. Cameroni, G. Fibriansah, J. Shi, T. Barca, I. Pagani, A. Rubio, V. Broccoli, E. Vicenzi, V. Graham, S. Pullan, S. Dowall, R. Hewson, S. Jurt, O. Zerbe, K. Stettler, A. Lanzavecchia, F. Sallusto, A. Cavalli, E. Harris, S.-M. Lok, L. Varani, D. Corti, A human bi-specific antibody against Zika virus with high therapeutic potential. *Cell* **171**, 229–241 e215 (2017).

17. L. Xu, Q. Zheng, S. Li, M. He, Y. Wu, Y. Li, R. Zhu, H. Yu, Q. Hong, J. Jiang, Z. Li, S. Li, H. Zhao, L. Yang, W. Hou, W. Wang, X. Ye, J. Zhang, T. S. Baker, T. Cheng, Z. H. Zhou, X. Yan, N. Xia, Atomic structures of Coxsackievirus A6 and its complex with a neutralizing antibody. *Nat. Commun.* **8**, 505 (2017).

18. G. Barba-Spaeth, W. Dejnirattisai, A. Rouvinski, M.-C. Vaney, I. Medits, A. Sharma, E. Simon-Lorière, A. Sakuntabhai, V.-M. Cao-Lormeau, A. Haouz, P. England, K. Stiasny, J. Mongkolsapaya, F. X. Heinz, G. R. Screaton, F. A. Rey, Structural basis of potent Zika–dengue virus antibody cross-neutralization. *Nature* **536**, 48–53 (2016).

19. Y. Dong, Y. Liu, W. Jiang, T. J. Smith, Z. Xu, M. G. Rossmann, Antibody-induced uncoating of human rhinovirus B14. *Proc. Natl. Acad. Sci. U.S.A.* **114**, 8017–8022 (2017).

20. J. M. Hogle, M. Chow, D. J. Filman, Three-dimensional structure of poliovirus at 2.9 A resolution. *Science* **229**, 1358–1365 (1985).

21. M. G. Rossmann, E. Arnold, J. W. Erickson, E. A. Frankenberger, J. P. Griffith, H.-J. Hecht, J. E. Johnson, G. Kamer, M. Luo, A. G. Mosser, R. R. Rueckert, B. Sherry, G. Vriend, Structure of a human common cold virus and functional relationship to other picornaviruses. *Nature* **317**, 145–153 (1985).

22. X. Wang, W. Peng, J. Ren, Z. Hu, J. Xu, Z. Lou, X. Li, W. Yin, X. Shen, C. Porta, T. S. Walter, G. Evans, D. Axford, R. Owen, D. J. Rowlands, J. Wang, D. I. Stuart, E. E. Fry, Z. Rao, A sensor-adaptor mechanism for enterovirus uncoating from structures of EV71. *Nat. Struct. Mol. Biol.* **19**, 424–429 (2012).

23. J. Ren, X. Wang, Z. Hu, Q. Gao, Y. Sun, X. Li, C. Porta, T. S. Walter, R. J. Gilbert, Y. Zhao, D. Axford, M. Williams, K. McAuley, D. J. Rowlands, W. Yin, J. Wang, D. I. Stuart, Z. Rao, E. E. Fry, Picornavirus uncoating intermediate captured in atomic detail. *Nat. Commun.* **4**, 1929 (2013).

24. W. A. Marasco, J. Sui, The growth and potential of human antiviral monoclonal antibody therapeutics. *Nat. Biotechnol.* **25**, 1421–1434 (2007).

25. P. Plevka, P.-Y. Lim, R. Perera, J. Cardosa, A. Suksatu, R. J. Kuhn, M. G. Rossmann, Neutralizing antibodies can initiate genome release from human enterovirus 71. *Proc. Natl. Acad. Sci. U.S.A.* **111**, 2134–2139 (2014).

26. S. Li, H. Zhao, L. Yang, W. Hou, L. Xu, Y. Wu, W. Wang, C. Chen, J. Wan, X. Ye, Z. Liang, Q. Mao, T. Cheng, N. Xia, A neonatal mouse model of coxsackievirus A10 infection for anti-viral evaluation. *Antiviral Res.* **144**, 247–255 (2017).

27. H. Lee, J. O. Cifuente, R. E. Ashley, J. F. Conway, A. M. Makhov, Y. Tano, H. Shimizu, Y. Nishimura, S. Hafenstein, A strain-specific epitope of enterovirus 71 identified by cryo-electron microscopy of the complex with fab from neutralizing antibody. *J. Virol.* **87**, 11363–11370 (2013).

28. N. Verdaguer, G. Schoehn, W. F. Ochoa, I. Fita, S. Brookes, A. King, E. Domingo, M. G. Mateu, D. Stuart, E. A. Hewat, Flexibility of the major antigenic loop of foot-and-mouth disease virus bound to a Fab fragment of a neutralising antibody: Structure and neutralisation. *Virology* **255**, 260–268 (1999).

29. Y. Liu, M. G. Hill, T. Klose, Z. Chen, K. Watters, Y. A. Bochkov, W. Jiang, A. C. Palmenberg, M. G. Rossmann, Atomic structure of a rhinovirus C, a virus species linked to severe childhood asthma. *Proc. Natl. Acad. Sci. U.S.A.* **113**, 8997–9002 (2016).

30. J. Ren, X. Wang, L. Zhu, Z. Hu, Q. Gao, P. Yang, X. Li, J. Wang, X. Shen, E. E. Fry, Z. Rao, D. I. Stuart, Structures of coxsackievirus A16 capsids with native antigenicity: Implications for particle expansion, receptor binding, and immunogenicity. *J. Virol.* **89**, 10500–10511 (2015).

31. J. K. Muckelbauer, M. Kremer, I. Minor, L. Tong, A. Zlotnick, J. E. Johnson, M. G. Rossmann, Structure determination of coxsackievirus B3 to 3.5 Å resolution. *Acta Crystallogr. D Biol. Crystallogr.* **51**, 871–887 (1995).

32. S. T. Miller, J. M. Hogle, D. J. Filman, *Ab initio* phasing of high-symmetry macromolecular complexes: Successful phasing of authentic poliovirus data to 3.0 Å resolution. *J. Mol. Biol.* **307**, 499–512 (2001).

33. Y. Liu, J. Sheng, A. Fokine, G. Meng, W.-H. Shin, F. Long, R. J. Kuhn, D. Kihara, M. G. Rossmann, Structure and inhibition of EV-D68, a virus that causes respiratory illness in children. *Science* **347**, 71–74 (2015).

34. X. Wang, J. Ren, Q. Gao, Z. Hu, Y. Sun, X. Li, D. J. Rowlands, W. Yin, J. Wang, D. I. Stuart, Z. Rao, E. E. Fry, Hepatitis A virus and the origins of picornaviruses. *Nature* **517**, 85–88 (2015).

35. K. L. Shingler, J. L. Yoder, M. S. Carnegie, R. E. Ashley, A. M. Makhov, J. F. Conway, S. Hafenstein, The enterovirus 71 A-particle forms a gateway to allow genome release: A cryoEM study of picornavirus uncoating. *PLOS Pathog.* **9**, e1003240 (2013).

36. H. Lee, K. L. Shingler, L. J. Organtini, R. E. Ashley, A. M. Makhov, J. F. Conway, S. Hafenstein, The novel asymmetric entry intermediate of a picornavirus captured with nanodiscs. *Sci. Adv.* **2**, e1501929 (2016).

37. C. Butan, D. J. Filman, J. M. Hogle, Cryo-electron microscopy reconstruction shows poliovirus 135S particles poised for membrane interaction and RNA release. *J. Virol.* **88**, 1758–1770 (2014).

38. Y.-X. Zhang, Y.-M. Huang, Q.-J. Li, X.-Y. Li, Y.-D. Zhou, F. Guo, J.-M. Zhou, S. Cen, A highly conserved amino acid in VP1 regulates maturation of enterovirus 71. *PLOS Pathog.* **13**, e1006625 (2017).

39. Z. Chen, E. R. Fischer, D. Kouiavskaia, B. T. Hansen, S. J. Ludtke, B. Bidzhieva, M. Makiya, L. Agulto, R. H. Purcell, K. Chumakov, Cross-neutralizing human anti-poliovirus antibodies bind the recognition site for cellular receptor. *Proc. Natl. Acad. Sci. U.S.A.* **110**, 20242–20247 (2013).

40. K. L. Shingler, J. O. Cifuente, R. E. Ashley, A. M. Makhov, J. F. Conway, S. Hafenstein, The enterovirus 71 procapsid binds neutralizing antibodies and rescues virus infection in vitro. *J. Virol.* **89**, 1900–1908 (2015).

41. X. Ye, C. Fan, Z. Ku, T. Zuo, L. Kong, C. Zhang, J. Shi, Q. Liu, T. Chen, Y. Zhang, W. Jiang, L. Zhang, Z. Huang, Y. Cong, Structural basis for recognition of human enterovirus 71 by a bivalent broadly neutralizing monoclonal antibody. *PLOS Pathog.* **12**, e1005454 (2016).

42. T. S. Walter, J. Ren, T. J. Tuthill, D. J. Rowlands, D. I. Stuart, E. E. Fry, A plate-based high-throughput assay for virus stability and vaccine formulation. *J. Virol. Methods* **185**, 166–170 (2012).

43. K. J. Livak, T. D. Schmittgen, Analysis of relative gene expression data using real-time quantitative PCR and the $2^{-\Delta\Delta C_T}$ method. *Methods* **25**, 402–408 (2001).

44. S. Q. Zheng, E. Palovcak, J.-P. Armache, K. A. Verba, Y. Cheng, D. A. Agard, MotionCor2: Anisotropic correction of beam-induced motion for improved cryo-electron microscopy. *Nat. Methods* **14**, 331–332 (2017).

45. K. Zhang, Gctf: Real-time CTF determination and correction. *J. Struct. Biol.* **193**, 1–12 (2016).

46. G. Tang, L. Peng, P. R. Baldwin, D. S. Mann, W. Jiang, I. Rees, S. J. Ludtke, EMAN2: An extensible image processing suite for electron microscopy. *J. Struct. Biol.* **157**, 38–46 (2007).

47. S. H. W. Scheres, RELION: Implementation of a Bayesian approach to cryo-EM structure determination. *J. Struct. Biol.* **180**, 519–530 (2012).

48. X. Yan, R. S. Sinkovits, T. S. Baker, AUTO3DEM—An automated and high throughput program for image reconstruction of icosahedral particles. *J. Struct. Biol.* **157**, 73–82 (2007).

49. S. H. W. Scheres, S. Chen, Prevention of overfitting in cryo-EM structure determination. *Nat. Methods* **9**, 853–854 (2012).

50. L. Swint-Kruse, C. S. Brown, Resmap: Automated representation of macromolecular interfaces as two-dimensional networks. *Bioinformatics* **21**, 3327–3328 (2005).

51. D. S. Biovia, Discovery studio modeling environment, release 4.5 (Dassault Systemes, San Diego, 2015).

52. E. F. Pettersen, T. D. Goddard, C. C. Huang, G. S. Couch, D. M. Greenblatt, E. C. Meng, T. E. Ferrin, UCSF Chimera—A visualization system for exploratory research and analysis. *J. Comput. Chem.* **25**, 1605–1612 (2004).

53. P. Emsley, B. Lohkamp, W. G. Scott, K. Cowtan, Features and development of *Coot*. *Acta Crystallogr. D Biol. Crystallogr.* **66**, 486–501 (2010).

54. P. D. Adams, P. V. Afonine, G. Bunkóczi, V. B. Chen, I. W. Davis, N. Echols, J. J. Headd, L.-W. Hung, G. J. Kapral, R. W. Grosse-Kunstleve, A. J. McCoy, N. W. Moriarty, R. Oeffner, R. J. Read, D. C. Richardson, J. S. Richardson, T. C. Terwilliger, P. H. Zwart, *PHENIX*: A comprehensive Python-based system for macromolecular structure solution. *Acta Crystallogr. D Biol. Crystallogr.* **66**, 213–221 (2010).

55. V. B. Chen, W. B. Arendall III, J. J. Headd, D. A. Keedy, R. M. Immormino, G. J. Kapral, L. W. Murray, J. S. Richardson, D. C. Richardson, MolProbity: All-atom structure validation for macromolecular crystallography. *Acta Crystallogr. D Biol. Crystallogr.* **66**, 12–21 (2010).

56. B. A. Barad, N. Echols, R. Y.-R. Wang, Y. Cheng, F. DiMaio, P. D. Adams, J. S. Fraser, EMRinger: Side chain–directed model and map validation for 3D cryo-electron microscopy. *Nat. Methods* **12**, 943–946 (2015).

57. P. Gouet, E. Courcelle, D. I. Stuart, F. Métoz, ESPript: Analysis of multiple sequence alignments in PostScript. *Bioinformatics* **15**, 305–308 (1999).

58. W. L. DeLano, The PyMOL molecular graphics system (2002); http://pymol.org.

59. C. Xiao, M. G. Rossmann, Interpretation of electron density with stereographic roadmap projections. *J. Struct. Biol.* **158**, 182–187 (2007).

60. Collaborative Computational Project, Number 4, The CCP4 suite: Programs for protein crystallography. *Acta Crystallogr. D Biol. Crystallogr.* **50**, 760–763 (1994).

Acknowledgments

Citation: R. Zhu, L. Xu, Q. Zheng, Y. Cui, S. Li, M. He, Z. Yin, D. Liu, S. Li, Z. Li, Z. Chen, H. Yu, Y. Que, C. Liu, Z. Kong, J. Zhang, T. S. Baker, X. Yan, Z. Hong Zhou, T. Cheng, N. Xia, Discovery and structural characterization of a therapeutic antibody against coxsackievirus A10. *Sci. Adv.* **4**, eaat7459 (2018).

ScienceAdvances

Discovery and structural characterization of a therapeutic antibody against coxsackievirus A10

Rui Zhu, Longfa Xu, Qingbing Zheng, Yanxiang Cui, Shaowei Li, Maozhou He, Zhichao Yin, Dongxiao Liu, Shuxuan Li, Zizhen Li, Zhenqin Chen, Hai Yu, Yuqiong Que, Che Liu, Zhibo Kong, Jun Zhang, Timothy S. Baker, Xiaodong Yan, Z. Hong Zhou, Tong Cheng and Ningshao Xia

ARTICLE TOOLS	http://advances.sciencemag.org/content/4/9/eaat7459
SUPPLEMENTARY MATERIALS	http://advances.sciencemag.org/content/suppl/2018/09/17/4.9.eaat7459.DC1
REFERENCES	This article cites 58 articles, 11 of which you can access for free http://advances.sciencemag.org/content/4/9/eaat7459#BIBL
PERMISSIONS	http://www.sciencemag.org/help/reprints-and-permissions

Use of this article is subject to the Terms of Service